



# Measurement Report: Atmospheric CH<sub>4</sub> at regional stations of the Korea Meteorological Administration/ Global Atmosphere Watch Programme: measurement, characteristics and long-term changes of its drivers

5

Haeyoung Lee\*, Won-Ick Seo, Shanlan Li, Soojeong Lee, Samuel Kenea, and Sangwon Joo

National Institute of Meteorological Sciences, Jeju, 63568, Republic of Korea

10 *Correspondence to Haeyoung Lee (leehy80@korea.kr)*

Abstract. To quantify CH<sub>4</sub> emissions at policy-relevant spatial scales, the Korea Meteorological Administration (KMA) started monitoring its atmospheric levels in 1999 at Anmyeondo (AMY), and expanded monitoring to Jeju Gosan Suwolbong (JGS) and Ulleungdo (ULD) in 2012. The monitoring system consists of a Cavity Ring Down Spectrometer (CRDS) and a new cryogenic drying method, with a measurement uncertainty (68% c.i.) of 0.7–0.8 ppb. To determine the regional characteristics of CH<sub>4</sub> at each KMA station, we assessed the CH<sub>4</sub> level relative to local background (CH<sub>4</sub>xs), analyzed local surface winds and CH<sub>4</sub> with bivariate polar plots, and investigated CH<sub>4</sub> diurnal cycles. We also compared the CH<sub>4</sub> levels measured at KMA stations with those measured at the Mt. Waliguan (WLG) station in China and Ryori (ROY) station in Japan. CH<sub>4</sub>xs followed the order AMY (55.3±37.7 ppb) > JGS (24.1±10.2 ppb) > ULD (7.4±3.9 ppb). Although CH<sub>4</sub> was observed in well mixed air at AMY, it was higher than at other KMA stations, indicating that it was affected not only by local sources but also by distant air masses. Annual mean CH<sub>4</sub> was highest at AMY among all East Asian stations, while its seasonal amplitude was smaller than at JGS, which was strongly affected in the summer by local biogenic activities. From the long-term records at AMY, we confirmed that the source of CH<sub>4</sub>xs changed from the past (2006 to 2010) to recent (2016 to 2020) years in East Asia. Especially in northern China, CH<sub>4</sub>xs was mainly attributed to fossil fuel combustion or biomass burning during 2006–2010, but mainly to biogenic activities during 2016–2020, as indicated by decreasing  $\delta^{13}\text{C}_{\text{CH}_4}$  from the northern China. CH<sub>4</sub> emissions in the southern part of China and in South Korea were enhanced by biogenic signals during 2016–2020. We confirmed that long-term high-quality data can help understand changes in CH<sub>4</sub> emissions in East Asia.

## 1. Introduction

Atmospheric methane (CH<sub>4</sub>) is an important greenhouse gas and is one of the main drivers of climate change on Earth. The global atmospheric CH<sub>4</sub> abundance was 1889±2 ppb in 2020, increasing 2.6 times since 1750 (~722 ppb, pre-industrial period); the relative CH<sub>4</sub> increase since pre-industrial is greater than other major greenhouse gases such as CO<sub>2</sub> (1.5 times) and nitrous oxide (1.2 times) (WMO, 2021). Recently, CH<sub>4</sub> has gained substantial interest because of its relatively shorter lifetime in the atmosphere (~ 9 year) compared with that of other long-lived greenhouse gases (Prinn et al., 2005). CH<sub>4</sub> emission reduction may thus be an



effective method to partially mitigate climate change. The 6<sup>th</sup> Intergovernmental Panel on Climate Change (IPCC) reported that, if strong and sustained CH<sub>4</sub> emission reductions are integrated with air pollution controls, net warming could decrease in the long term because of the short lifetime of both CH<sub>4</sub> and aerosols (IPCC, 2021).

To reduce the atmospheric CH<sub>4</sub> burden, its emissions and sinks must first be quantified. CH<sub>4</sub> loss is primarily attributed to reaction with hydroxyl radicals (OH), which are part of atmospheric photochemical cycles, while there are various natural (wetlands, freshwaters, and geological) and anthropogenic CH<sub>4</sub> sources (agriculture, waste, fossil fuels, and biomass burning) with different spatial and temporal distributions (Jackson et al., 2020, Lan et al., 2021). Because of its diverse sources in different regions, high resolution, quality data can help quantify the atmospheric CH<sub>4</sub> budget.

In the World Meteorological Organization (WMO), Global Atmosphere Watch Programme (GAW), there are 170 stations that monitor atmospheric CH<sub>4</sub>, but with poor spatial coverage in Asia (gawsis.meteoswiss.ch, last access: November 2021).

Among CH<sub>4</sub> sources, rice agriculture is intense in Asia, mainly in China and India (Kai et al., 2011). China has also the largest anthropogenic CH<sub>4</sub> emissions in the world (Janssens-Maenhout et al., 2019). South Korea ranks among the world's top three importers of liquefied natural gas (LNG), following Japan and China (eia.gov/international/analysis/country/KOR. last access: November 2021). In this regard, the Korean atmospheric monitoring network is important to understand not only South Korea CH<sub>4</sub> burden but also Asia continent because of its location, as it is sensitive to air masses transported from Asia, and especially from China.

South Korea's atmospheric CH<sub>4</sub> monitoring history started at Tae-Ahn Peninsula (TAP, 36.74°N, 126.13°E, 20 m above sea level) by Korea Centre for Atmospheric Environment Research in the western part of Korea in 1990, with weekly flask-air sample collection as a part of the U.S. National Oceanic and Atmospheric Administration (NOAA), Global Monitoring Laboratory (GML), Cooperative Global Air Sampling Network (<http://www.esrl.noaa.gov/gmd/ccgg/flask.php>). Since 1999, the Korea Meteorological Administration (KMA) has been monitoring atmospheric CH<sub>4</sub> with quasi-continuous measurements at Anmyeondo (AMY, 36.53°N, 126.32°E, a 40 m tower whose base is 46 m above sea level), approximately 28 km from TAP. In 2012, KMA expanded its monitoring network to capture data from the south-west (Jeju Gosan Suwolbong, JGS, 33.30°N, 126.16°E) and east (Ulleungdo, ULD, 37.48°N, 130.90°E) of Korea to cover the entire peninsula for a better understanding of CH<sub>4</sub> sources and its characteristics. However, there is no published description of measurement quality, regional characteristics and long-term trends of CH<sub>4</sub> for Korea network.

A few studies reported that CH<sub>4</sub> levels are affected by emissions from Russian wetlands and local rice cultivation near TAP (Dlugokencky et al., 1993; Kim et al., 2014). In 2019, observations at AMY indicate larger emissions compared with previous years, which were caused by soil temperature and moisture changes (Kenea et al., 2021). In summer, high atmospheric CH<sub>4</sub> levels were observed in airborne measurements because of biogenic sources such as rice paddies, landfills, and livestock (Li et al., 2020). A large ratio, CH<sub>4</sub>/C<sub>2</sub>H<sub>6</sub>, was observed during KORUS-AQ campaign from May to June 2016 in the vicinity of industrial regions in west coast of South Korea (Li et al., 2022). These findings are related to the case studies so that it can be difficult to figure out the representative long-term and regional characteristics in Korea. Also even if CH<sub>4</sub> is monitored at regional scale during long-term period, poor measurement quality can lead to misinterpretation of the CH<sub>4</sub> budget, preventing development of science-based policies. Additionally, both measurement uncertainty and inadequate assessment of background air can limit the accuracy of observation-based estimates for local or regional scale greenhouse gas emissions (Graven et al., 2012; Turnbull et al., 2009, 2015; Lee et al., 2019).

In this paper, we present CH<sub>4</sub> data quality procedures and processing methods at three KMA monitoring stations, including measurement uncertainties. We analyzed the characteristics of CH<sub>4</sub> at the KMA stations from 2016 to 2020 and compared the data



with those collected at other stations in East Asia: the global background WMO/GAW station in Waliguan (WLG, 36.28°N, 100.90°E, 3810 m), China; and the WMO/GAW station at Ryori (RYO, 39.03°N, 141.82°E, 260 m) in Japan, which reflects the global growth rate (Watanabe et al., 2000). In addition, we investigated the changes in CH<sub>4</sub> enhancement from 1999 to 2021 and analyzed the source regions based on measurements of  $\delta C_{(CH_4)}$  in flask-air samples to trace the major source changes. Furthermore, this study can serve as a reference for KMA data archived at the World Data Centre for Greenhouse Gases.

## 2. Experiment

### 2.1 Sampling sites

The locations of AMY, JGS, and ULD stations are shown in Fig. 1 and summaries of the measurement systems are in Table 1. Detailed information was provided in Lee et al. (2019). Only key information focusing on CH<sub>4</sub> is summarized here.

AMY is located in the western part of Korea approximately 28 km south from TAP and 130 km southwest from the megacity of Seoul. Within 50 km of AMY, the second largest rice paddies and largest livestock industry of Korea are present. The largest coal and heavy oil fired thermal power plants in Korea are present within 35 km of this station, to the north-east and south-east, respectively, and the largest LNG power plant in Korea is 100 km to the north east of this station. The local region mainly consists of agricultural land growing rice, sweet potatoes, and onions, and the area is also known for its leisure opportunities during summer. The west and south sides of AMY are open to the sea, with a large tidal mudflat with many pine trees along the coast.

JGS is located in the western part of Jeju Island, which is the largest volcanic island (1,845.88 km<sup>2</sup>) in the south-west of Korea and is approximately 90 km from the mainland. The major industries here are tourism and livestock, which focuses on horses and pigs. JGS is located within a famous Global Geo-park that has outcrops of volcanic deposits exposed along the coastal cliff. Next to JGS, agriculture is widespread, with potatoes, garlic, and onions being the main crops in the largest plain in Jeju Island. The station is open to the sea from the south-west to north-west, with the cliffs comprising volcanic basalt rocks. The sea to the south is connected to the East China Sea and the sea to the west is linked to the Yellow Sea.

ULD is located in the east of Ulleung Island, which is in the eastern part of Korea and approximately 155 km from the mainland. In the south-eastern part of the Korea Peninsula, numerous steel, chemical, and petrochemical industries are present along the coastline, within approximately 200–250 km from the island. There are two large natural gas power plants. Ulleung Island covers 72 km<sup>2</sup>, and has a volcanic origin, being a rocky steep-sided island that is the top of a large stratovolcano that has a maximum elevation of 984 m. This peak is located northwest of ULD. There are a few small mountains with heights from 500 to 960 m a.s.l., within 5 km to the north and southeast of the station. Because of those geological features, ULD is mainly affected by airflow from over the hill to the southwest and by downslope winds from northeast. Before 2016, there was a garbage incineration plant 300 m from ULD. In the southwestern area, there is a small brickyard 200 m from the station and a garbage incinerator within 100 m. The garbage incineration facility was moved to the north side of island in December 2016. Therefore, many studies do not include the data before 2017. Farming and fishing industries are very active on the island, although there are no farms in the southern area. An automatic weather station (AWS) was installed at AMY near the air sampling inlet, and 10 m above the station at JGS and ULD, independent from the air inlet tower.



Figure 1. Locations of KMA CH<sub>4</sub> monitoring stations in Korea: Anmyeondo (AMY), Jeju Gosan Suwolbong (JGS) and Ullengdo (ULD). Tae-an Peninsula (TAP, 36.74°N, 126.13°E), part of NOAA's flask-air sampling network, is 28 km from AMY in South Korea. Mt. Waliguan (WLG, 36.28°N, 100.90°E) and Ryori (RYO, 39.03°N, 141.82°E) are located in China and Japan, respectively. This map is derived from google map.

## 2.2 Measurement environment and instrument

At all three stations, the measurement system consists of 1) inlet, 2) pump, 3) drying system, and 4) analyzer. Detailed information of the system was discussed by Lee et al. (2019).

1) Inlet: Dekabon sampling tubing (Nitta Moore 1300-10, I.D. 6.8 mm, O.D. 10 mm, high-density polyethylene jacket, overlapped aluminum tape, and ethylene copolymer liner) with a stainless-steel filter (D 4.7 cm, pore size 5 μm) mounted on a plastic mesh holder is installed on the intake and connected to the pump. The inlet height was changed at AMY in 2004 and at JGS in 2017 (Table 1).

2) Pump: A KNF diaphragm pump (N145.1.2AN.18, Germany, 55 L/min, 7 bar in AMY; N035AN.18, Germany, 30 L/min, 4 bar in JGS and ULD) is installed between the inlet and drying system.

3) Drying system: Sample air is dried with a cryogenic method (CT-90, Operon, Korea, -90°C). Inside the drying system, there are two chambers with two steps; ambient air is cooled to -20°C in the first chamber, and then to -50°C in the second chamber. This system was installed in 2012 at all three KMA stations.

4) Analyzer: A model G2301 (Picarro, USA) was installed in October 2011, and it became the official CH<sub>4</sub> measurement system at AMY starting February 1, 2016. Before February 2016 (G2301), a GC-FID was used to monitor atmospheric CH<sub>4</sub>. CRDS records atmospheric CH<sub>4</sub> every 5 s across the KMA Greenhouse Gas (GHG) network while the GC-FID measured CH<sub>4</sub> every 30 min. At JGS, the monitoring of atmospheric CH<sub>4</sub> started with the use of G1301 in 2012, which was changed to G2401 from 2020. G2401 has been used from 2012 at ULD.



Table 1. Information on the three KMA CH<sub>4</sub> monitoring stations in Korea

Station (ID)	Longitude Latitude Altitude	Inlet height (period)	Instrument Model (period)	Drying method (period)	Standard scale (period)
Anmyeondo (AMY)	126.32°E 36.53°N 47 m a.s.l	20 m (1999 to 2004)	GC-FID (1999 to 2016 Feb)	Three step dehumidification system 1) -4°C cold trap 2) Nafion™ 3) Mg(ClO <sub>4</sub> ) <sub>2</sub> (1999 to 2011)	KRISS (1999 to 2011)  WMO-X2004A (2012 to present)
		40 m (since 2004)	CRDS 2301 for CO <sub>2</sub> and CH <sub>4</sub> (2016 Feb to present)	Cryogenic system (since 2012)	
Jejudo Gosan Suwolbong (JGS)	126.16°E 33.30°N 71.47 m a.s.l	6 m (2012 to 2017)	CRDS 1301 for CO <sub>2</sub> and CH <sub>4</sub> (2012 to 2019)	Cryogenic system	WMO-X2004A (2012 to present)
		12 m (since 2017)	CRDS 2401 for CO <sub>2</sub> , CH <sub>4</sub> , and CO (since 2020)		
Ulleungdo* (ULD)	130.90°E 37.48°N 220.9 m a.s.l	10 m (since 2012)	CRDS 2401 for CO <sub>2</sub> , CH <sub>4</sub> , and CO (since 2012)	Cryogenic system	WMO-X2004A (2012 to present)

\*ULD is not registered in the GAW network.

### 5 2.3 Calibration method

Our highest level standards are designated “laboratory standards”. We have four laboratory standards prepared by the WMO GAW Central Calibration Laboratory (CCL) on the WMO-X2004A scale in the range 1700 to 2500 ppb with uncertainties of less than 2 ppb (95% confidence level, coverage factor k=2, gml.noaa.gov/ccl/ch4).

For working standards, dry, ambient air is compressed into a cylinder at AMY with a range of roughly 1800-2500 ppb. To bracket the measurement range, we diluted collected air to around 1700 ppb with pure zero air.

Filled working standards are sent to a central laboratory of the National Institute of Meteorological Sciences (NIMS) in Jeju for calibration against the laboratory standards. The scale was transferred with a CRDS (G2401, Picarro, USA). The scale propagation uncertainty is described in section 3.1. Normally the difference in H<sub>2</sub>O between laboratory and working standards measured by CRDS is ~0.00054%, which leads to a bias of 0.01 to 0.014 ppb for CH<sub>4</sub> in the given range according to the Eq. (1) from Rella et al. (2013). This value is negligible so it was not considered as a factor for the propagated uncertainty (Eq. 1)

$$\frac{C_{dilution}}{C_{dry}} = 1 - 0.01H_{act} \quad (\text{Eq. 1})$$

where  $C$  is the CH<sub>4</sub> mole fraction and  $H_{act}$  is the actual water mole fraction (in %). Here  $H_{act}$  is the H<sub>2</sub>O difference between standard gases and samples.



Analyzer response had been calibrated every two weeks for all stations before 2019 Dec. but it was changed to 5 or 6 days with different calibration frequency at each station based on the reproducibility; all 4 working standard gases with a range of 1700-2500 ppb at intervals of 200-300 ppb were measured by the CRDS for 40–50 min. Only the last 10 min of data were used for the calibration of CH<sub>4</sub> to ensure instrument stability (Lee et al., 2021). Our ability to maintain and propagate the WMO-2004A scale

5 was shown through the 6<sup>th</sup> Round Robin comparison test (RR) of standards hosted by the CCL ([https://www.esrl.noaa.gov/gmd/ccgg/wmorr/wmorr\\_results.php](https://www.esrl.noaa.gov/gmd/ccgg/wmorr/wmorr_results.php), the difference for low CH<sub>4</sub> levels was  $0.7 \pm 0.7$  ppb while that for high CH<sub>4</sub> levels was  $0.6 \pm 0.7$  ppb)

When we started monitoring atmospheric CH<sub>4</sub> at AMY in 1999, the GC-FID response was calibrated every 1.5 h with a 1-point calibration against the KRISS scale until February 2016. During this period, we used standards that were certified directly by  
10 KRISS without working standards. KRISS and WMO-2004A scales agreed well with a difference from -0.1 to 0.8 ppb ([gml.noaa.gov/webdata/ccgg/wmorr/rr5](http://gml.noaa.gov/webdata/ccgg/wmorr/rr5), last access: Jun 2022). WMO round robin comparison of standard scales (Round robin number 5) included measurements with our GC-FID; differences with the CCL were from -0.3 to 1.3 ppb in the range 1756 to 1819 ppb.

## 15 2.4 Data quality control/assurance process and baseline selection method

### 2.4.1 Auto and manual quality control/assurance process

All data were collected and stored at NIMS in Jeju, Korea. Raw data at 5 s intervals (L0 data) were processed as L1 data with 1) auto flagging and 2) manual flagging. Auto flagging involved 6 criteria, including instrument malfunction, instrument detection limit, and value outside the given calibration range. Manual flags were assigned by technicians at each station according to the  
20 logbook based on inlet filter exchange, diaphragm pump error, low flow rate, dehumidification system error, calibration periods, experimental periods such as participation in comparison experiments, observatory environmental issue such as construction next to a station, extreme weather, or other issues related to the instrument. These codes refer to definitions by the World Data Centre for reactive gases and aerosols maintained by EBAS for the GAW Programme (<http://www.nilu.no/projects/ccc/flags/flags.html>, last access: 23 Aug. 2022) that were modified for the Korea network. Data with flags were reviewed by scientists at NIMS, and  
25 only valid data were averaged into Level 2 (L2) hourly average data. To define valid data, all data were compared between South Korea stations and other global stations at similar latitude to Korea.

One of the way of quality assurance, a co-located comparison of discrete samples collected at AMY, the sampled flasks were analyzed by NOAA/GML and compared with our in-situ analyzer results. This comparison between L2 hourly data from the CRDS and weekly flask-air samples collected at AMY has been ongoing since December 2013. The mean difference, flask minus CRDS  
30 hourly mean in situ, was  $2.2 \pm 11.8$  ppb from 2016 to 2020, which is close to GAW's compatibility goal for CH<sub>4</sub> ( $\pm 2$  ppb) (Fig. S1). During the period of GC-FID measurements, the average difference ( $\pm 1$  SD) between KMA and NOAA flasks was  $5.2 \pm 15.6$  ppb, which is greater than the difference since CRDS observations started but reasonable as per the GAW extended compatibility goal of  $\pm 5$  ppb.





#### 2.4.2 Regional background selection method

To understand the atmospheric CH<sub>4</sub> measurements and CH<sub>4</sub> growth rate, data representing well-mixed air should be selected for analysis on a regional scale. There are many methods to select data for baseline such as using related tracers, AWS data, or statistical methods (Fang et al., 2015; Chambers et al., 2016; Bacastow et al., 1985; Lowe et al., 1979). For Korea network, we used a statistical method and it was described in detail by Seo et al. (2021). There are three criteria; 1) hourly standard deviation (HS), 2) differences in consecutive hourly values (CD) and standard deviation of a 30-day moving average (MS). After applying HS and CD to observed data, the data were defined as L3 hourly data. Even though the data were selected by HS and CD, high CH<sub>4</sub> levels remained because of long-lasting stagnant conditions (e.g. over 6 days). Therefore, we also apply MS (Table 2). MS was multiplied by  $\alpha$ , which was determined empirically. This process retained 21–52% of the data at each station, which were defined as L3 hourly and daily data based on observations. The method developed by Thoning et al. (1989) was used to fit smooth curves to L3 daily averages. These curves reduce noise induced by synoptic-scale atmospheric variability, fill measurement gaps, and are used to represent the regional baseline. Finally, we can get the L3 monthly data, long-term trend and seasonal amplitude, which indicates the magnitude of the peak to trough of the detrended seasonal cycle, after applying Thoning et al. (1989).

Table 2. Criteria and percentage of selected background levels from observed data at each station. HS: Hourly standard deviation, CD: consecutive hourly value, MS: standard deviation of a 30-day moving average

Station ID	AMY	JGS	ULD
Data period	1999 to 2020	2012 to 2020	2014 to 2020
HS [ppb]	2.1	2.1	2.8
CD [ppb]	4.9	5.2	3.6
MS [ppb]		1.8 $\sigma_{30d}$	
Spring, MAM [%]	29.1	46.6	57.9
Summer, JJA [%]	11.0	33.5	37.6
Autumn, SON [%]	16.9	30.9	53.2
Winter, DJF [%]	28.4	49.1	58.9
Total [%]	21.3	40.64	52.2

CH<sub>4</sub> data were produced from 2016 under the same conditions for all three stations; however, ULD was affected by emissions from a garbage incinerator until Dec. 2016, while AMY was affected by a malfunction of the drying system for 26 Aug-9 Sep. 2016. The garbage incinerator was moved to the northeast part of the island in December 2016. Therefore, we compared data from the three stations from 2016 to 2020, excluding the periods mentioned above.

In section 3.5, for comparison of our station annual/monthly mean and seasonal amplitude to those parameters calculated from other Asian stations (Mt. Waliguan global GAW station (WLG, 100.90°E, 36.28° N, 3810 m) and Ryori regional GAW station (RYO, 141.82° E, 39.03° N, 260 m)), we downloaded daily data for these stations from the World Data Centre for Greenhouse



Gases (<http://gaw.kishou.go.jp>). We applied the Thoning et al. (1989) method to each daily data set to get annual/monthly mean and seasonal amplitude to compare.

## 2.5 Flask-air data

5 Long-term data on CH<sub>4</sub> and its isotopes ( $\delta^{13}\text{C}$  in CH<sub>4</sub>, hereafter  $\delta^{13}\text{C}_{(\text{CH}_4)}$ ) were collected at TAP, 24 km away from AMY. Samples were collected weekly between 1200 and 1800 (Korea Local Time), when boundary layer height (BLH) was maximum. The collected samples were sent to Boulder, Colorado for measurement of CH<sub>4</sub> at NOAA and to INSTAAR (Institute of Arctic and Alpine Research, University of Colorado) for  $\delta^{13}\text{C}_{(\text{CH}_4)}$  analysis. Samples were analyzed from 1990 for CH<sub>4</sub> and from 2000 for  $\delta^{13}\text{C}_{(\text{CH}_4)}$ . Since TAP and AMY are only 24 km apart, their data are representative of the same region under large synoptic  
10 conditions, especially for well mixed air. These data were thus used to trace the changes in the surrounding environment in East Asia (section 3.5). AMY started sampling in December 2013 and these data were used only for characterization of CH<sub>4</sub> at AMY in section 3.5.

## 2.6 Hybrid Single-Particle Lagrangian Integrated Trajectory model (HYSPPLIT) cluster analysis

15 We downloaded and installed the HYSPLIT with window version and used the built-in algorithm. HYSPLIT trajectories were calculated using the Global Data Assimilation and Prediction System (GDAPS) at a horizontal resolution of 25 km to determine the origin of air masses transported to TAP during 2005–2020. The back trajectories were calculated for 96 h periods at 3 h intervals, with 500 m altitude matching the time of each flask-air sample. Based on a cluster analysis, northern China (CN) accounted for 27% of all air masses; these originated in Russia and travelled through Mongolia and northeast China. Southern China (CS)  
20 accounted for 6%; these air masses originated from East China sea and the southern part of China. Air masses from Korea local (KL) reflected emissions from the Korean Peninsula and Japan, accounting for 17% of the total air masses. Other sectors were also analyzed, but there were no significant or representative changes in emissions, so they are not reported herein.

## 2.7 Potential Source Strength (PSS) analysis

25 We calculated PSS using the trajectory statistics approach, which has often been applied to estimate the potential source areas of air pollutants (Remann et al., 2004, 2008; Li et al., 2017). The trajectory statistics approach calculates air mass residence time weighted mean mole fractions for target compounds (CH<sub>4</sub> in this study) for the domain with  $0.5^\circ \times 0.5^\circ$  grids using the following formula (Eq. 2):  
30

$$\overline{C}_{(i,j)} = \frac{\sum_{a=1}^M T_{(i,j,a)} C_a}{\sum_{a=1}^M T_{(i,j,a)}} \quad (\text{Eq. 2})$$

where  $C(i, j)$  represents the potential source strength of the cell  $i, j$  as a potential source region of the target compound (CH<sub>4</sub>);  $a$  is the index of the trajectory;  $M$  is the total number of trajectories that passed through cell  $i, j$ ;  $C_a$  is the enhanced mole fraction (difference from background mole fractions mentioned in section 3.2 below) measured during the arrival of trajectory  $a$ ; and  $T_{i,j,a}$





is the residence time of trajectory a spent over grid cell  $i, j$ . Residence times were calculated using the method described by Poirot and Wishinski (1998). To consider the influence of air masses on emissions at ground level, the air masses passing above the BLH were excluded. BLH was obtained from the HYSPLIT model. To exclude the influences of emission sources surrounding AMY, enhanced CH<sub>4</sub> data with wind speeds lower than 2 m/s were excluded from the PSS analysis.

## 5 3. Results and Discussion

### 3.1 Measurement uncertainty

Observed CH<sub>4</sub> is influenced by natural atmospheric variability and measurement procedures. Natural atmospheric variability can be represented as the standard deviation of all measurements contributing to a time-average, after the contribution of experimental noise is accounted for. The measurement uncertainty is critical to provide information on data quality so that users can understand the limitations and reliability of values. According to previous studies, the total measurement uncertainty consists of multiple uncertainty components (Andrews et al., 2014, Verhulst et al., 2017). For the KMA network, a measurement uncertainty of approximately 0.11 ppm has been calculated for CO<sub>2</sub> with limited but practical components (Lee et al., 2019). Using the same method used for CO<sub>2</sub>, we calculated a practical realistic measurement uncertainty for CH<sub>4</sub> in the KMA network (Eq.3). Based on the measurement of target cylinders and a co-located comparison of measurements at AMY and JGS, we assumed systematic biases to be negligible (<http://empa.ch/web/s503/wcc-empa>, last access: January 2022).

$$(U_T)^2 = (U_{h_2o})^2 + (U_p)^2 + (U_r)^2 + (U_{scale})^2 \quad (\text{Eq. 3})$$

where  $U_T$  is the total measurement uncertainty in the reported dry-air mole fractions;  $U_{h_2o}$  is the uncertainty from the drying system;  $U_p$  is repeatability;  $U_r$  is reproducibility; and  $U_{scale}$  is the uncertainty of propagating the WMO-X2004A CH<sub>4</sub> scale to working standard gases.

Since working standards had nearly the same level of H<sub>2</sub>O as laboratory standards through the CRDS, we only considered the CH<sub>4</sub> dilution offsets between standards and sample air while estimating the uncertainty.  $U_{h_2o}$  was computed from the differences in H<sub>2</sub>O (%) between the ambient airstream through the drying system and standard gases injected directly, bypassing the drying system. An ideal measurement would be through the analysis of the standard gases and air samples after they pass through the same drying system (WMO, 2016). However, our drying efficiency was not constant, so we injected standard gases directly as a reference value of H<sub>2</sub>O. We defined hourly mean H<sub>2</sub>O values from standard gases in the calibration period as a reference value. This value was applied to ambient air to calculate  $U_{h_2o}$  before the next calibration. This meant that the uncertainty component was time dependent. Eq.(1) was applied to this factor, where  $H_{act}$  was the difference between H<sub>2</sub>O in samples and standard gases. Hourly CH<sub>4</sub> dilution maximum offsets are up to 0.009 ppb at AMY, 0.006 ppb at JGS and 0.009 ppb at ULD from 2016 to 2020. Since positive and negative values were found, we used the following equation (Eq. 4):

$$U_x = \sqrt{\frac{\sum_{i=1}^N (x_i)^2}{N}} \quad (\text{Eq. 4})$$

35



where  $U_x$  represents  $U_{h2o}$ ;  $x$  is the hourly  $CH_4$  dilution offsets from Eq(1);  $N$  is the total number of hourly mean values.  $U_{h2o}$  is tabulated for each station in table 3. This uncertainty term was smallest (0.006 to 0.008 ppb) among all uncertainty factors in the KMA network.

5 We expressed  $U_r$  as the standard deviation of all drift during the experimental period using Eq (4), where  $U_x$  represents  $U_r$ ;  $x_i$  is the drift occurring between calibration episodes; and  $N$  is the total number of data. They are tabulated with other uncertainty terms by site in table 3. We determined  $U_r$  as the differences in  $CH_4$  measured from cylinders with subsequent calibrations after two weeks. It ranged from  $-0.9$  to  $2$  ppb at AMY and from  $-1.25$  to  $0.84$  ppb at JGS. ULD had a two week calibration periods, which changed to one month from May 18, 2017 to November 11, 2019. During this period of one month calibration frequency,  $U_r$  increased to  
10 maximum of  $4$  ppb, which is greater than the WMO/GAW compatibility goal of  $\pm 2$  ppb. After conducting the reproducibility test in November 2019, the calibration frequency decreased to 5 days. Therefore,  $U_r$  at ULD was separated into two groups including or excluding the period with a longer calibration period (with asterisk in Table 3). When we considered only the period with a higher calibration frequency, the uncertainty at ULD was similar to that at other stations. This means that  $U_r$  is the largest component of measurement uncertainty, and that  $U_T$  can be decreased using an appropriate calibration strategy.

15

$U_p$  was determined from the standard deviations of working standard measurements, as described in section 2.3, and expressed by a pooled standard deviation (Eq. 5).

$$U_p = \sqrt{\frac{\sum_{i=1}^N N_i \times S_i^2}{N_i - N_t}} \quad (\text{Eq. 5})$$

20

where  $S_i$  is the standard deviation of 10 min averages of working standard measurements;  $N_i$  the index number of a measurement during 10 min (based on 5 s intervals); and  $N_t$  is the total number of calibrations during the period.  $S_i$  was less than 0.882 ppb at AMY, 0.603 ppb at JGS, and 0.688 ppb at ULD. The pooled standard deviations ( $U_p$ ) are shown in table 3.

25 According to Zhao et al. (2006), the uncertainty of working standards can be calculated by the propagation error arising from the uncertainty of primaries with a maximum propagation coefficient ( $\gamma = 1$ ) and repeatability. Similarly,  $U_{scale}$  for working standards is determined by (Eq. 6)

$$U_{scale} = \sqrt{U_p^2 + U_{lab}^2} \quad (\text{Eq. 6})$$

30

where  $U_{lab}$  is the uncertainty of laboratory standards, which CCL (NOAA/GML) certified. Here,  $U_{lab}$  has the same value as the uncertainty of secondary standards, 0.3 ppb with a confidence interval of 68%, based on calibration of the secondary standards against the primary standards ([http://gml.noaa.gov/ccl/ch4\\_scale.html](http://gml.noaa.gov/ccl/ch4_scale.html), last access: January 2022). These values were the same for all stations since they were calibrated by a central lab at NIMS in Jeju. Therefore,  $U_p$  is the repeatability at the central lab since we  
35 propagated the standard scale through the same analyzer and set-up for atmospheric monitoring. This value was always less than 0.12 ppb.



Table 3. Uncertainty estimates for measurements of CH<sub>4</sub> at each station from 2016 to 2020. Units are ppb. All terms are 68% confidence intervals

Uncertainty terms	AMY	JGS	ULD
U <sub>h2o</sub>	0.006	0.006	0.008
U <sub>p</sub>	0.157	0.120	0.351
U <sub>r</sub>	0.578	0.365	2.323 (0.710*)
U <sub>scale</sub>	0.323	0.323	0.323
U <sub>T</sub>	0.778	0.728	2.352 (0.801*)

\*This value was calculated excluding the period with one-month calibration frequency

5

For AMY, the difference from the CCL in the RR test with the analysis of the same cylinder was from -0.3 to 1.3 ppb with GC-FID in 2010. Therefore, we considered the largest value of 1.3 ppb as the measurement uncertainty from 1999 to February 2016 during the GC-FID measurement period.

10 Overall, the total measurement uncertainty was calculated to be from 0.728 to 0.801 ppb. These values were similar to those reported by CRDS measurements (< 1 ppb) (Winderlich et al., 2010; Andrews et al., 2014, Verhulst., 2017). In the future, quoted uncertainties could be greater owing to the inclusion of more error sources, while repeatability and reproducibility may improve with a different calibration strategy.

### 3.2 Local/regional effects on observed CH<sub>4</sub>

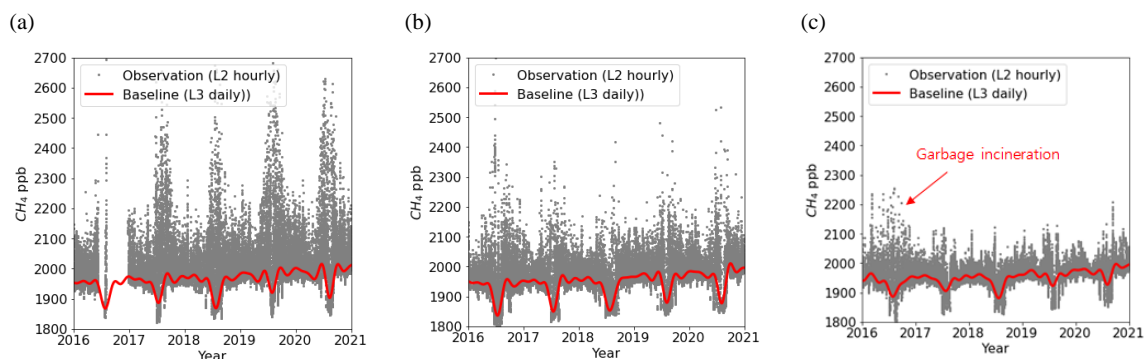
15 The enhancement of CH<sub>4</sub> relative to the regional background can help evaluate local/regional additions to CH<sub>4</sub>, with the excess signal defined as (Eq. 7):

$$\text{CH}_{4\text{XS}} = \text{CH}_{4\text{OBS}} - \text{CH}_{4\text{BG}} \quad (\text{Eq. 7})$$

20 where CH<sub>4OBS</sub> is L2 hourly data (before filtering) and CH<sub>4BG</sub> indicates the regional background at a site as determined by the smoothed curve fitted to L3 daily data (section 2.4.2). CH<sub>4XS</sub> was greatest in the order AMY (55.3±37.7 ppb) > JGS (24.1±10.2 ppb) > ULD (7.4±3.9 ppb) from 2016 to 2020. For ULD, we excluded data collected in 2016 as they were affected by the garbage incinerator next to the station (section 2.4, Figure 2(c)). All stations showed largest CH<sub>4XS</sub> in summer (June, July, August) with 109.6 ± 23.8 ppb at AMY, 37.0 ± 2.1 ppb at JGS and 12.2 ± 3.7 ppb at ULD. Conversely, the smallest values were observed as  
25 25.6 ± 2.4 ppb at AMY and 18.8 ± 4.1 ppb at JGS in spring (March, April, May), while the lowest value of 7.5 ± 0.4 ppb at ULD was observed in winter (December, January, February). The baseline selection conditions listed in Table 2 also supported this result. The selected baseline data accounted for only 11–37.6% of summer data at all stations, indicating that CH<sub>4</sub> levels were



elevated in summer. In winter and spring, we could better capture well mixed air compared with other seasons (28.4–58.9%) because of the strong westerly wind with Siberian high.



5 Figure 2. L2 hourly (grey scatters, observation) and fitted L3 daily data (red line, Baseline) at (a) AMY, (b) JGS, and (c) ULD from 2016 to 2020.

To understand the influence of local surface wind on observed CH<sub>4</sub>, bivariate polar plots were used for 2018. These plots express the dependence of all hourly CH<sub>4</sub> (L2 hourly data) on wind direction and speed (Fig. 3–5). The wind data were derived from an AWS, as described in section 2.1.

10

At AMY, when wind speed was consistently  $< 3 \text{ m}\cdot\text{s}^{-1}$ , CH<sub>4</sub> was elevated during all seasons. Especially in summer, it showed strong signals when wind direction was between  $45^\circ$  and  $135^\circ$  (from land). A similar observation was made in other seasons, possibly indicating that this was related to local influences such as from rice paddies. The dominant wind direction was south-west in summer and north-west in winter. Even though lower CH<sub>4</sub> levels were captured regardless of wind direction with increased wind speed, CH<sub>4</sub>s was still higher than that at the other two stations. Therefore, AMY could be affected not only by local activities but also by distant emissions.

15

JGS experienced the strongest winds among the three stations in all seasons (maximum  $27.5 \text{ m}\cdot\text{s}^{-1}$ ). Strong north-westerly wind (open sea) occurred in spring and winter, and air masses from the north-east (Korean inland) were noted during autumn and from the south (open sea) during summer. CH<sub>4</sub> was lower than at AMY, with strong signals observed in all seasons under different criteria. Higher CH<sub>4</sub> levels occurred because of winds from the eastern part of JGS in autumn and summer when the wind speed decreased to less than  $5 \text{ m}\cdot\text{s}^{-1}$ . For spring and winter, strong signals were noted in the eastern and northern parts of JGS. Since JGS is located downwind from continental Asia and strong westerly winds occur in winter/spring because of the strong Siberian high, this signal might be related to activities not only in Asia but also in Jeju.

20

For ULD, the main wind directions were quite clearly from  $0^\circ$  to  $90^\circ$  (30%) and from  $180^\circ$  to  $270^\circ$  (33%), and wind speeds less than  $5 \text{ m}\cdot\text{s}^{-1}$  occurred 72% of the total time. High CH<sub>4</sub> episodes were mainly observed when the wind direction was between  $180^\circ$  and  $225^\circ$ , presumably affected by the southeastern part of the Korean Peninsula. This wind direction was very dominant in summer with a lower wind speed than that in other seasons.

25

Overall, atmospheric CH<sub>4</sub> observed by KMA GAW stations was affected not only by the local area but also by air masses from continental Asia, as indicated by the results from synoptic systems. Signals at AMY may be affected by local/regional activities,



such as agriculture and livestock industries, owing to the relatively lower wind speeds; however, it still showed higher values compared with those of other stations when it captured well-mixed air. This indicates that AMY was affected not only by local sources but also by long range transport of air masses originating from continental Asia. ULD showed lower CH<sub>4</sub> and was less affected by local impacts.

5

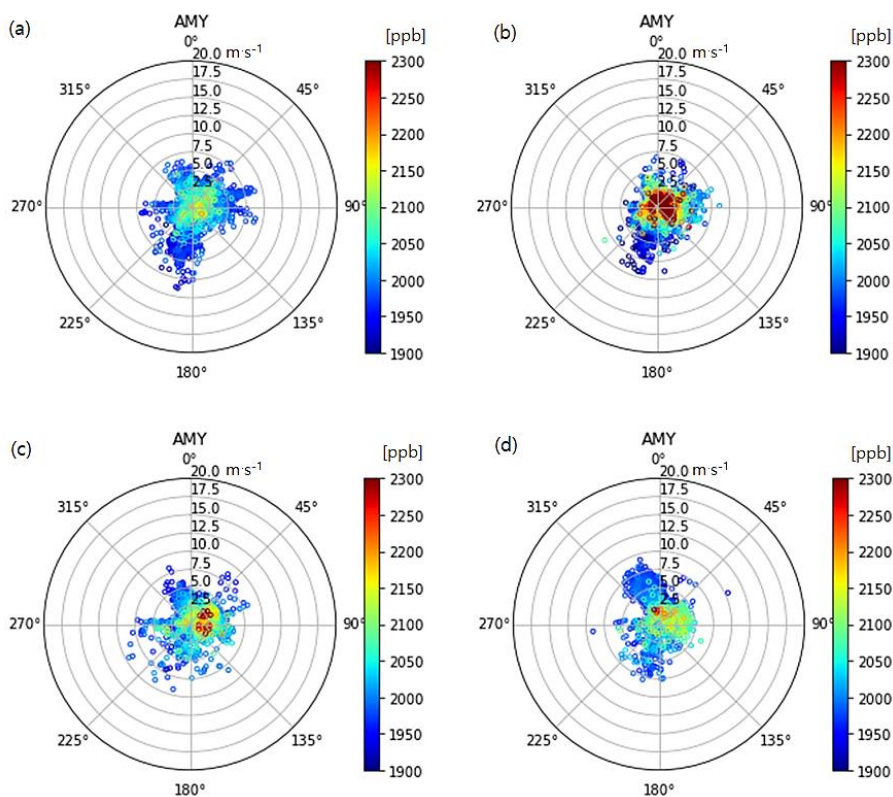


Figure 3. Bivariate polar plots for observed CH<sub>4</sub> (L2 hourly) in spring (a), summer (b), autumn (c), and winter (d) at AMY in 2018.

10

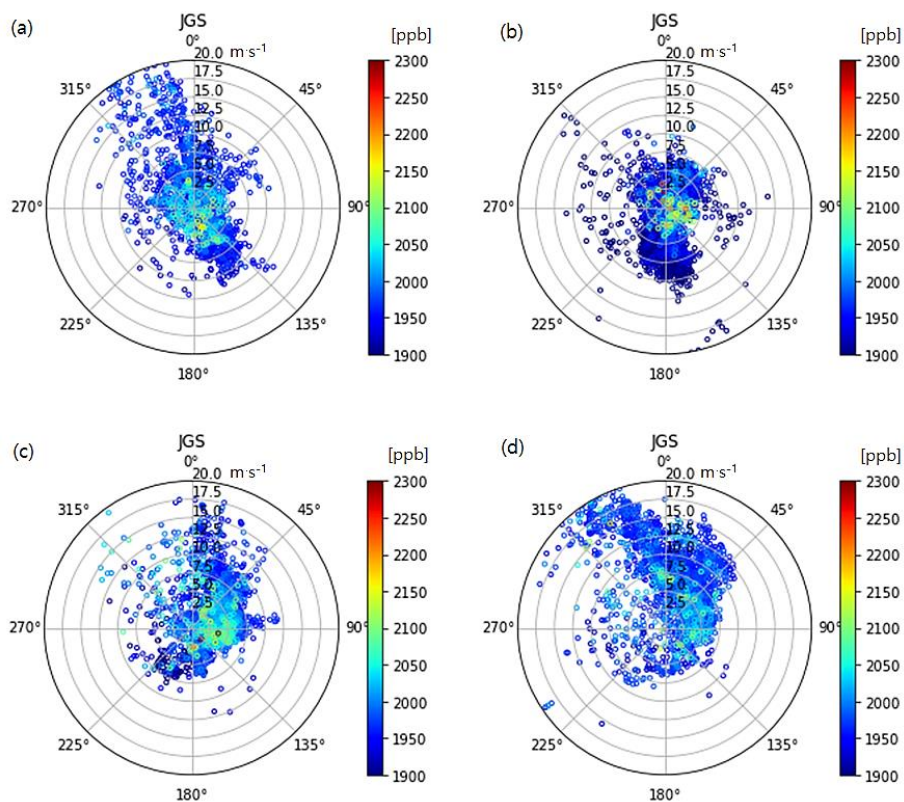


Figure 4. Bivariate polar plots for observed CH<sub>4</sub> (L2 hourly) in spring (a), summer (b), autumn (c), and winter (d) at JGS in 2018.



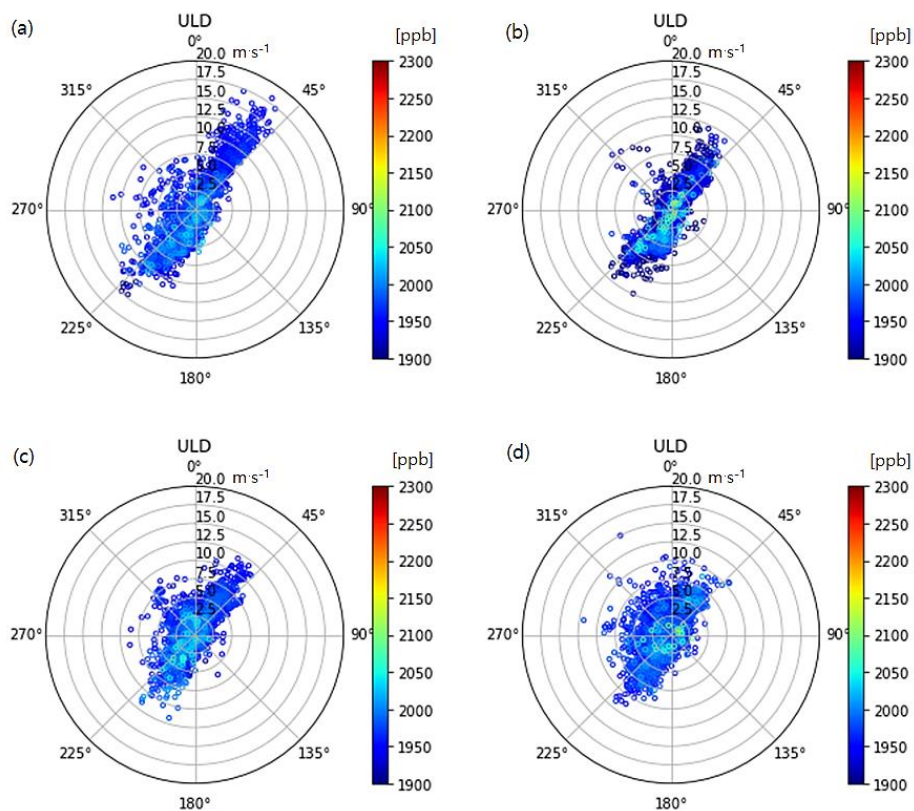


Figure 5. Bivariate polar plots for observed CH<sub>4</sub> (L2 hourly) in spring (a), summer (b), autumn (c), and winter (d) at ULD in 2018.

### 3.3 Average diurnal variation

5 Diurnal CH<sub>4</sub> variations were calculated as the average deviation from the daily mean in each month from L2 hourly data from 2016 to 2020 (recent 5 years) for AMY and JGS, and from 2017 to 2020 for ULD (Fig. 6).

Among the three stations, the mean diurnal variation of all seasons was greatest at AMY (69.5±49 ppb) and smallest at ULD (7.6±4.2 ppb), while it was 24.7±14.4 ppb at JGS. Daily variations in CH<sub>4</sub> are generally small at global scale stations, so stations with a large seasonal cycle amplitude may be affected by local/regional sources (Aoki et al., 1992) and transport driven such as upslope/downslope air and land/see breeze due to geographical reason.

AMY was surrounded by CH<sub>4</sub> sources as described in the introduction, while ULD had similar characteristics to global scale stations that are less impacted by their local/regional environment. Similar to ULD, Mt. Waliguan station (3816 m), a representative global GAW station in Asia, also showed an amplitude of 5 to 10 ppb for the diurnal CH<sub>4</sub> cycle (Zhou et al. 2004., Fang et al., 2013).

15 Atmospheric CH<sub>4</sub> at AMY and JGS started to increase around midnight and peaked from 5 to 8 AM local time and then decreased with minimum value from 15 PM to 17 PM. For ULD, the peaks were observed between 6 to 11 AM, especially in summer, but there were no significant troughs. These variations at AMY and JGS were consistent with the changes in wind pattern and BLH.



BLH was maximum near the middle of the day. At night, radiation loss at ground level leads to a stable boundary layer, leading to accumulation of CH<sub>4</sub> (Worthy et al., 1998, Higuchi et al., 2003). Both stations were also affected by land-see-breeze and received air from seaside during the daytime, which enhanced the diurnal variation. These patterns of CH<sub>4</sub> were similar to those of CO<sub>2</sub> observed by both stations (Lee et al., 2019) because of similar meteorological conditions. However, ULD is located on the slope of the mountain and is surrounded by a complex terrain, thus being affected by certain winds from north to east and south to west, regardless of time and season. However, peak values only occurred during 6 to 11 AM, which needs further study.

All stations showed the lowest amplitude in winter (Dec. to Feb.) and the largest amplitude in summer (Jun to Aug.). AMY showed the largest diurnal amplitude ( $176.8 \pm 74.6$  ppb) in August among the three stations, which was almost 2.5 times greater than the annual mean value, with substantial variation among months. JGS and ULD showed the largest amplitude in August ( $43.4 \pm 17.7$  ppb) and July ( $17.2 \pm 11.6$  ppb), respectively. This indicated that the emission and meteorological impacts (e.g. maximized BLH and land-see breeze) were strong in summer. AMY is close to rice paddies (110 km<sup>2</sup>), which are the major source of CH<sub>4</sub> in summer. JGS and ULD are not close to waterlogged paddies. However, high temperatures stimulate greater emissions from sources such as agriculture, livestock, and wetlands, thus affecting emissions at both stations. Similar to the observation made at AMY, previous studies have shown large variation in CH<sub>4</sub> emissions from the rice paddy area ( $196 \pm 65$  ppb) and wetland (~150 ppb) during summer (Worthy et al. 1998., Fang et al., 2013).

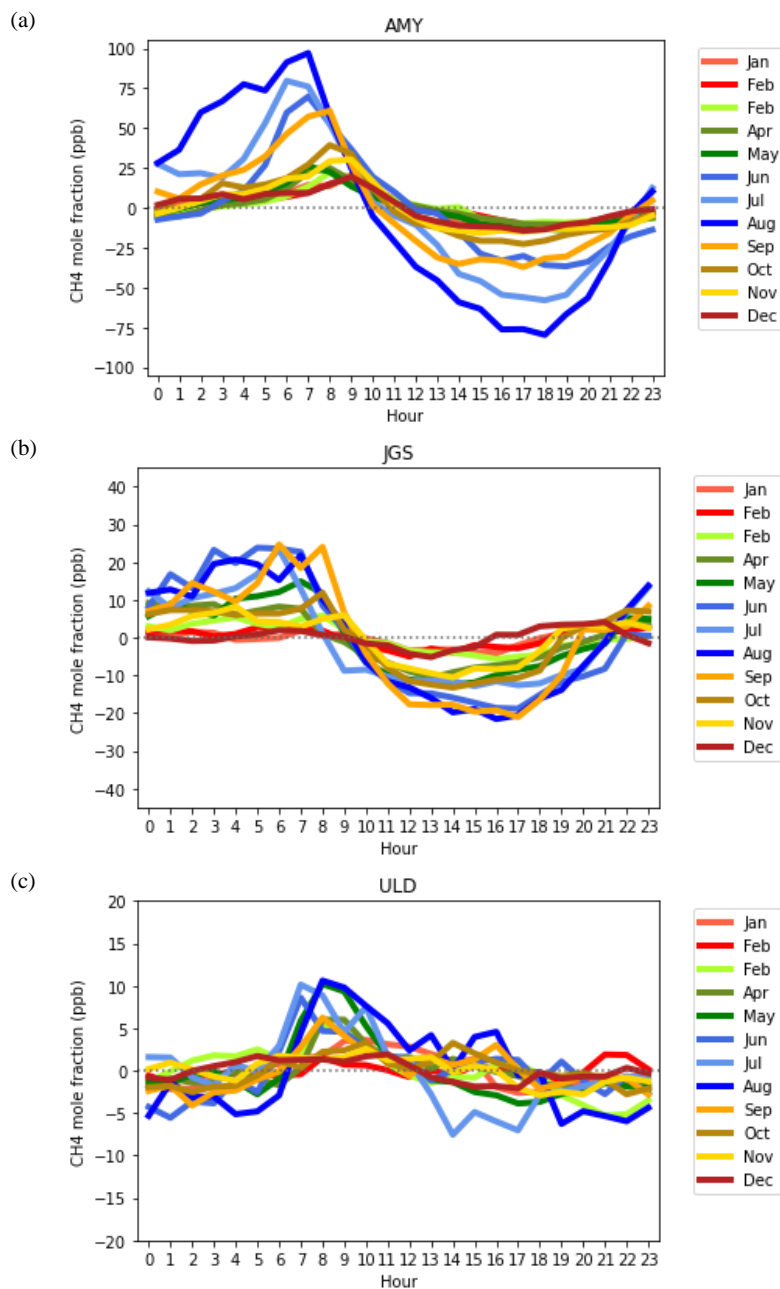


Figure 6. Mean diurnal variations of CH<sub>4</sub>. Values show the average departure from the daily mean in each month at (a) AMY and (b) JGS from 2016 to 2020 and (c) at ULD from 2017 to 2020.



### 3.4 Comparison with other East Asian stations: annual mean, seasonal amplitude, and growth rate

#### 3.4.1 Annual mean

Time series of monthly mean CH<sub>4</sub> from KMA's three stations and the two other stations in East Asia are compared in Fig. 7(a) and annual mean CH<sub>4</sub> is summarized in Table 4. Annual CH<sub>4</sub> mean was the highest at AMY and the lowest at WLG. The other stations showed similar levels of annual mean considering standard deviations. It was obvious that AMY was affected by local and regional activities, while WLG was affected by representative air masses of the Northern Hemisphere.

#### 3.4.2 Seasonal amplitude

As described in section 2.4, the seasonal amplitudes of CH<sub>4</sub> from 2016-2020 was calculated for three KMA stations and are compared with those values from WLG and RYO (Table 4). The seasonal amplitude is related to the combination of CH<sub>4</sub> surface flux distribution and chemical loss by reactions with OH and by soil loss. Seasonal amplitudes followed the order JGS > AMY > ULD > RYO > WLG (Table 4).

Since WLG is a global baseline station that is affected less by regional sources and sinks, the amplitude was smaller compared with the other regional stations. The amplitude of WLG was similar to that of other global stations such as Mauna Loa (30.6±4.2 ppb) (Dlugokencky et al., 1995). Seasonal amplitudes at AMY and JGS are much greater than at other 3 stations, and even inland regional stations in China, such as Lin'an (77±35 ppb) and Longfenshan (73±8 ppb) (Fang et al., 2013). Minimum values at JGS are -14.8±9.2 ppb lower than AMY minimum values while the maximum values at both stations are similar. Li et al. (2018) reported the summer air mass was affected by large-scale low-level monsoonal circulation across the tropic in Jeju. A similar meteorological impact for CH<sub>4</sub> was reported at TAP (28 km away from AMY) (Dlugokencky et al., 1993). Even though transport and OH radical can result in low CH<sub>4</sub> values at AMY during, the station is also affected by nearby sources with enhanced emissions during summer. As we introduced in section 2.1, AMY has large rice paddies and livestock industries within 50 km. During summer, high temperatures will enhance CH<sub>4</sub> emissions from these sources, leading to higher CH<sub>4</sub> than that at JGS (Kenea et al., 2021; Wang et al., 2021). Among regional stations, ULD and RYO may have been less affected by regional flux because of their altitude, causing their amplitude to be greater than that of WLG but smaller than that of AMY or JGS.

Minimum values were observed in summer, while maximum values occurred in spring, autumn, or winter for different regional stations. In contrast, WLG showed maximum levels in summer and minimum values in winter/spring. Zhang et al. (2013) reported that regional/local sources and air masses from polluted regions influenced by industry, crop residue burning, and agriculture may affect CH<sub>4</sub> observations at WLG in summer.

30

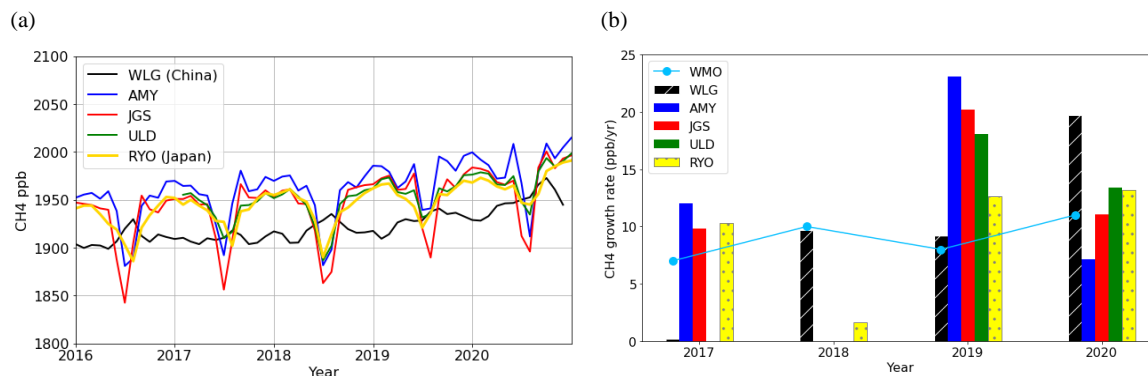


Figure 7. Time series of (a) monthly mean CH<sub>4</sub> and (b) annual growth rate at WLG, AMY, JGS, ULD, and RYO. The growth rate reported by WMO (WMO, 2021) is overlaid on (b) and this value is calculated as the change in annual mean from the previous year.

5

Table 4. Annual mean CH<sub>4</sub> with standard deviations from monthly mean from 2016 to 2020, mean seasonal amplitudes, and growth rates. Seasonal cycle amplitude during each calendar year was magnitude of the peak to trough of the detrended seasonal cycle (see section 2.4.2). The growth rate is an annual increase (not de-seasonal), absolute difference from previous year. Growth rate at ULD was calculated only from 2017 to 2020. Units are dry-air mole fractions (ppb)

Year	WLG	AMY	JGS	ULD	RYO
2016	<b>1909±9</b>	1942±28	1928±33	-	1929±19
2017	<b>1909±4</b>	<b>1954±24</b>	<b>1938±31</b>	<b>1942±15</b>	<b>1939±15</b>
2018	1919±9	<b>1953±31</b>	<b>1937±35</b>	<b>1941±24</b>	<b>1941±21</b>
2019	1928±10	1976±19	1957±26	1959±13	1954±14
2020	1948±14	1983±27	1968±32	1972±17	1967±14
Mean seasonal amplitude over 5 years.	21±5	100±13	118±9	67±12	58±8
Mean annual growth rate over 5 years (ppb·yr <sup>-1</sup> )	10±8	10±10	10±9	10±10	10±5

10

### 3.4.3 Growth rate

The annual growth rate was calculated by absolute difference from previous year (not de-seasonal) (Fig.7 (b)). When we analyzed the overall growth rate for 5 stations, mean values of annual growth rate from 2017 to 2020 were around 10 ppb·yr<sup>-1</sup>, which was similar to the WMO global mean (9±2 ppb·yr<sup>-1</sup>). However, when yearly comparisons were made, WLG and the other 4 regional stations varied. Especially from 2016 to 2017, WLG showed no increase in CH<sub>4</sub>, while CH<sub>4</sub> at other stations increased from 2017

15



to 2018. Normally the growth rate in CH<sub>4</sub> at WLG matches well with the WMO global trend (Fig. 7. (b)). Wang et al.(2021) reported that CH<sub>4</sub> fluxes in Asia are influenced by ENSO and temperature; therefore, we compared the growth rate of CH<sub>4</sub> from four regional stations with both factors (Fig. S2). This showed that the pattern of growth rate was quite similar to that of ENSO; however, even though the ENSO was negative (e.g., from 2017 to 2018) when surface temperature was high, the growth rate still increased. Plots of  $\delta^{13}\text{C}_{(\text{CH}_4)}$  vs  $1/\text{CH}_4$  had intercepts (indicating  $\delta^{13}\text{C}_{(\text{CH}_4)}$  source signatures of the enhancements) of  $-52.3\pm 2.2\%$  in winter and  $-53.7\pm 0.7\%$  in summer at AMY during 2016 to 2020 (Fig. S3). These values are very similar to the observed values during the summer vegetation period when biogenic emissions are very active ( $-52.5\pm 1.9\%$ ) in Europe (Varga et al., 2021), indicating that AMY was mainly affected by biogenic sources regardless of the season during this period. Throughout Asia, emissions from agriculture and waste account for over 50% of the total, which is increasing every year (Jackson et al., 2020). Since climate variability such as ENSO and temperature drive biogenic sources, the CH<sub>4</sub> growth rates observed at regional stations in Asia are more sensitive to regional emissions than the global station.

### 3.5 Long-term records of CH<sub>4</sub> and its drivers in East Asia

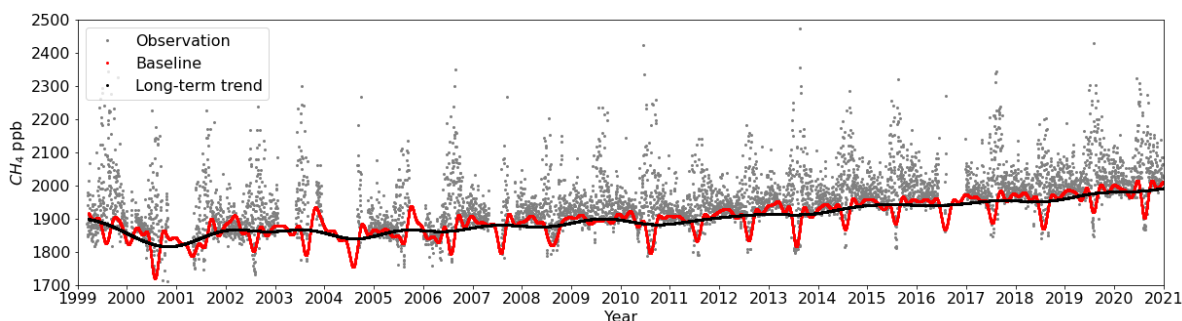


Figure 8. Time series of CH<sub>4</sub> (L2 daily, grey), baseline (L3 daily, red), and long-term trend (black) observed at AMY from 1999 to 2020.

The CH<sub>4</sub> trend is defined as upward growth in the data with the seasonal cycle removed (Thoning et al., 1989). The long-term trend at AMY was very similar to the global trend. From 1999 to 2005, the mean annual CH<sub>4</sub> growth rate (absolute differences from the previous year) was approximately  $-1.2 \text{ ppb}\cdot\text{yr}^{-1}$  at AMY, while the global value was  $0.3 \text{ ppb}\cdot\text{yr}^{-1}$  and both values have increased since 2006. CH<sub>4</sub> increased by  $3.3 \text{ ppb}\cdot\text{yr}^{-1}$  from 2006 to 2010 (global:  $5.9 \text{ ppb}\cdot\text{yr}^{-1}$ ) and by  $8.3 \text{ ppb}\cdot\text{yr}^{-1}$  (global:  $9 \text{ ppb}\cdot\text{yr}^{-1}$ ) from 2016 to 2020, indicating that the growth rate is accelerating. CH<sub>4</sub>xs did not vary much and was  $49\pm 74 \text{ ppb}$  during 2006–2010 and  $50\pm 70 \text{ ppb}$  during 2016–2020.

For PSS analysis with hourly CH<sub>4</sub>xs, however, the source distribution changed between 2006–2010 and 2016–2020 (Figure 9 (a) and (b)). We found that CH<sub>4</sub>xs from CS and KL were enhanced and remain constant respectively while that from CN became weaker in 2016–2020 compared with that in 2006–2010. This means that source region characteristics related to CH<sub>4</sub>xs had





changed. Sources affecting CS and KL paddy fields and that for CN was reported to be fossil fuel emissions (Zhang et al., 2011, Ito et al., 2022).

Using TAP  $\delta^{13}\text{C}_{(\text{CH}_4)}$  long-term measurements, keeling plots indicated that emissions from CN were mainly related to fossil fuel or biomass burning ( $-40.5 \pm 3.2\text{‰}$ ), while CS ( $-56.9 \pm 3.2\text{‰}$ ) and KL ( $-54.6 \pm 2.3\text{‰}$ ) were affected more by biogenic sources

5 during 2006–2010 (Fig.9 (c) and (d)). Sherwood et al. (2017) reported unweighted global mean  $\delta^{13}\text{C}$  of  $-44.8 \pm 10.7\text{‰}$  from fossil fuel use,  $-26.2 \pm 4\text{‰}$  from biomass burning, and  $-61.7 \pm 6.2\text{‰}$  from microbial sources. Even though the uncertainty of isotopic source signature is quite large,  $\text{CH}_4$  formed at high temperature such as combustion is enriched in the heavier isotope while  $\text{CH}_4$  from wetland, rice paddies and livestock is depleted. Air masses from CN were affected by several sources, however, this area was mainly related to pyrogenic and fossil fuel emissions as per the enriched  $\delta^{13}\text{C}_{(\text{CH}_4)}$  compared to that of other sectors.

10 During 2006–2010,  $\delta^{13}\text{C}_{(\text{CH}_4)}$  at CN and KL presented no significant trend, while the value observed at CS decreased.

However, we can confirm that  $\delta^{13}\text{C}_{(\text{CH}_4)}$  in all three sectors showed a range from  $-52.2 \pm 2.7\text{‰}$  to  $-49.5 \pm 2.7\text{‰}$  during 2016–2020, indicating that the  $\text{CH}_4$  sources in East Asia were mostly biogenic sources, although CN presented a fossil-fuel related source.

The decreasing trend of  $\delta^{13}\text{C}_{(\text{CH}_4)}$  at CN, CS, and KL also supports this assumption with lower values compared with those in 2006–2010 (Figure 9.(e) and (f)). Since coal emissions decreased from 2010 in China (Liu et al., 2021) and temperature impacts biogenic  $\text{CH}_4$  emissions, the major drivers of  $\text{CH}_4$  may have shifted from fossil fuel/biomass burning to biogenic sources such as wetlands and rice paddies.

Overall, AMY and global growth rates were renewed in 2006 and during 2006–2010; the increasing trend could be linked to mixed biogenic and fossil fuel sources in East Asia. However, the recent accelerated increase in  $\text{CH}_4$  emissions during 2016–2020 is more related to biogenic sources such as agriculture and wetland (Jackson et al., 2020, Lan et al., 2021).

20

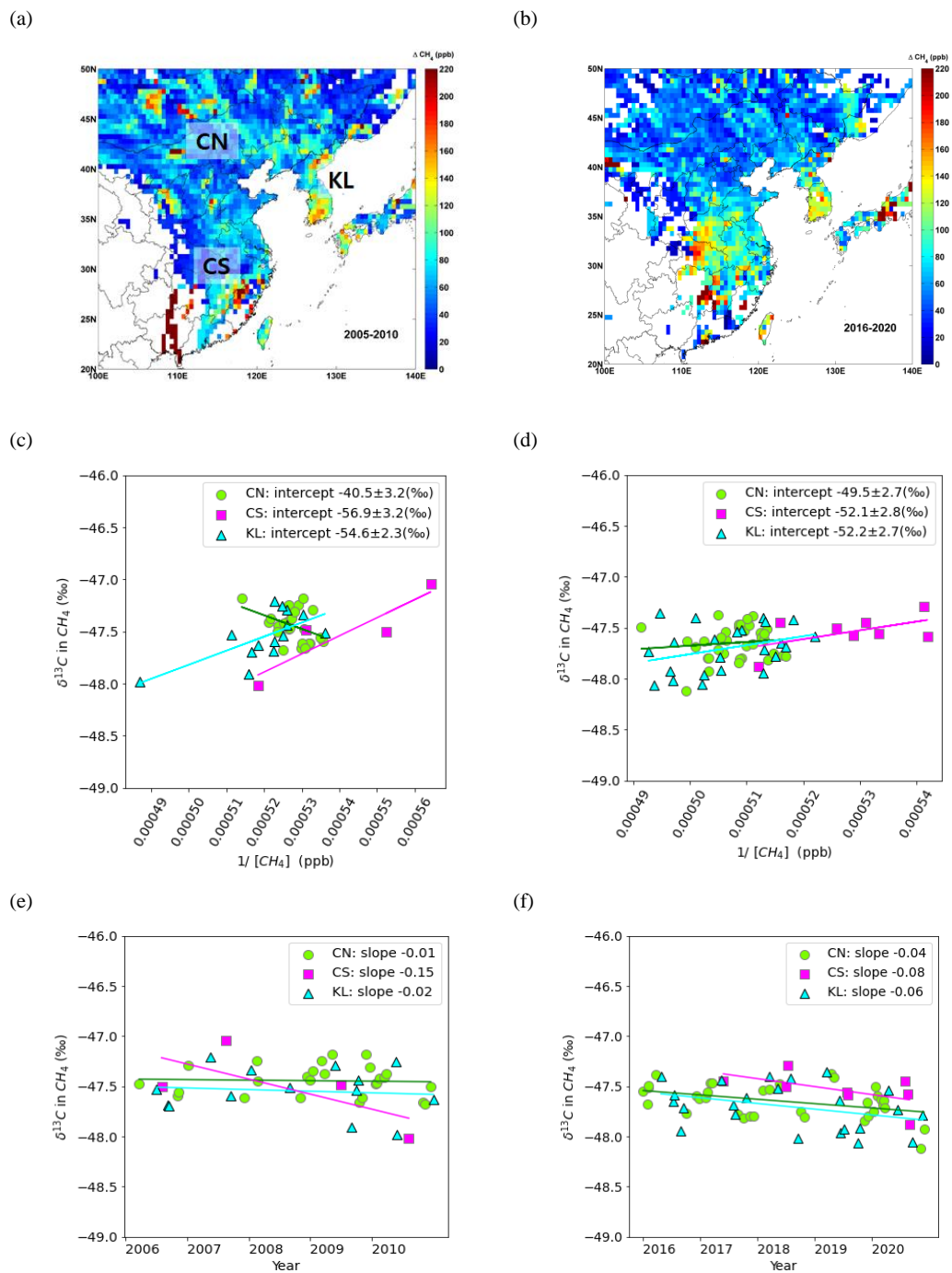


Figure 9. PSS analysis from (a) 2006 to 2010 and (b) 2016 to 2020. “Keeling” plots for (c) 2006 to 2010 and (d) 2016 to 2020. Time series of  $\delta^{13}\text{C}(\text{CH}_4)$  from (e) 2006 to 2010 and (f) 2016 to 2020.



#### 4. Summary and Conclusions

Among greenhouse gases, CH<sub>4</sub> emission reductions can be highly effective for short-term global warming mitigation because of its relatively short lifetime. However, its sources are diverse and yet to be evaluated completely through high accuracy measurements. Our study analyzed CH<sub>4</sub> characteristics observed at regional KMA GAW stations, uncertainties related to its measurement, and changes in sources using long-term data in South Korea.

KMA started monitoring atmospheric CH<sub>4</sub> in 1999 at AMY and expanded its network to the south and east parts of Korea at JGS and ULD in 2012 using a new system consisting of CRDS and a cryogenic drying system.

All three stations have similar measurement uncertainty from 2016 to 2020, in the range of 0.728–0.801 ppb. These uncertainties are similar to values reported in previous studies (less than 1 ppb). In addition, we confirmed reproducibility as the greatest contributor to measurement uncertainty; therefore, calibration strategies are the most critical component for reducing measurement uncertainty.

CH<sub>4xs</sub> assessed relative to local background levels at each station was in the order AMY (55.3±37.7 ppb) > JGS (24.1±10.2 ppb) > ULD (7.4±3.9 ppb). CH<sub>4xs</sub> was greatest in summer and lowest in spring or winter. This result is consistent with wind direction and speed. In summer, local biogenic sources affected observed CH<sub>4</sub>. Low wind speed enhanced CH<sub>4xs</sub>, while lower CH<sub>4</sub> levels were observed when the stations experienced high wind speed. For AMY, even when CH<sub>4</sub> was measured in well-mixed air, its level was higher than that at other stations, indicating that it was affected not only by local sources but also by distant air masses from Asia. ULD showed representative CH<sub>4</sub> levels without local impacts. Diurnal variations were greatest at AMY and smallest at ULD, and were affected by local sources and meteorological characteristics. The variation at ULD was 7.6±4.2 ppb, a value similar to that at the WLG baseline station in China (5 to 10 ppb). All stations had large diurnal cycles in summer, indicating a strong influence of local biogenic sources.

When CH<sub>4</sub> seasonal cycle amplitudes measured at KMA stations were compared with those at other East Asian stations from 2016 to 2020, the following descending order was observed: JGS (103±10) > AMY (85±16) > ULD (58±12) and RYO (57±12) > WLG (30±11). As discussed, since AMY reflected strong local influences not only in winter but also in summer, its seasonal amplitude was smaller than that of JGS. However, the annual CH<sub>4</sub> mean was the highest at AMY and lowest at WLG. The relative contributions of CH<sub>4</sub> source types to signals at regional stations in Asia are sensitive to temperature and ENSO. Based on analysis of δ<sup>13</sup>C(CH<sub>4</sub>) measurements, we established an increase in CH<sub>4</sub> from biogenic sources.

From the long-term analysis of CH<sub>4</sub> data at AMY, average CH<sub>4</sub> growth rate was 3.3 ppb·yr<sup>-1</sup> during 2006–2010, but increased to 8.3 ppb·yr<sup>-1</sup> in 2016–2020. However, CH<sub>4xs</sub> was similar while the source distribution was different based on our PSS analysis during each period. We infer significant changes in air masses arriving from our northern China sector. During 2006–2010, the main sources contributing to the CH<sub>4</sub> observations were fossil fuel and pyrogenic. The main sources shifted to biogenic/natural during 2016–2020. CH<sub>4</sub> emissions in the southern part of China and in local regions in Korea also had an enhanced biogenic/natural source signal.



#### Data availability

Atmospheric CH<sub>4</sub> data in KMA network are from HL and can be downloaded from climate.go.kr/home/09\_monitoring/search/search. TAP CH<sub>4</sub> and δ<sup>13</sup>C(CH<sub>4</sub>) data can be downloaded from https://doi.org/10.15138/VNCZ-M766/. RYO (DOI, https://gaw.kishou.go.jp/search/file/0001-2012-1002-01-01-9999) and WLJ (DOI, https://doi.org/10.15138/VNCZ-M766) data are downloaded from World Data Centre for Greenhouse Gases.

#### Author contributions

HL designed, wrote this paper and analyzed the data. WIS implemented the data QA/QC. SL implemented PSS analysis. SL run the central calibration centre for KMA stations and provide the calibration strategy. WIS, SL, SL, SK and SJ reviewed the manuscript. All authors contributed this work.

#### Acknowledgments.

We appreciate all staff and technicians at AMY, JGS, ULD in the Korea meteorological network, WLJ in China and RYO in Japan. Also special thanks to Dr. Ed Dlugokencky at NOAA and Dr. Silvia Michel at Colorado University for the support of this study. This work was funded by the Korea Meteorological Administration Research and Development Program “Development of Integrated Climate Change Monitoring and Analysis Techniques” under Grant (KMA2018-00324).

#### References

- Aoki, S., T. Nakazawa, S. Murayama, and S. Kawaguchi, Measurement of atmospheric methane at the Japanese Antarctic Station, Syowa, Tellus, Ser. B, 44, 273–281, doi:10.1034/J.1600-0889.1992.t01-3-00005. 1992
- Andrews, A. E., J. D. Kofler, M. E. Trudeau, J. C. Williams, D. H. Neff, K. A. Masarie, D. Y. Chao, D. R. Kitzis, P. C. Novelli, C. L. Zhao, E. J. Dlugokencky, P. M. Lang, M. J. Crowell, M. L. Fischer, M. J. Parker, J. T. Lee, D. D. Baumann, A. R. Desai, C. O. Stanier, S. F. J. De Wekker, D. E. Wolfe, J. W. Munger, P. P. Tans: CO<sub>2</sub>, CO, and CH<sub>4</sub> measurements from tall towers in the NOAA Earth System Research Laboratory’s Global Greenhouse Gas Reference Network: instrumentation, uncertainty analysis, and recommendations for future high-accuracy greenhouse gas monitoring efforts, Atmos. Meas. Tech., 7, 647–687, 2014
- Bacastow, R. B., C. D. Keeling, and T. P. Whorf, Seasonal amplitude increase in atmospheric CO<sub>2</sub> concentration at Mauna Loa, Hawaii, 1959–1982. J. Geophys. Res. Atmos., 90, 10529–10540, doi:10.1029/JD090iD06p10529. 1985
- Chambers, S. D., and Coauthors, Towards a universal “Baseline” characterisation of air masses for high and low-altitude observing stations using radon-222. Aerosol Air Qual. Res., 16, 885–899, doi:10.4209/aaqr.2015.06.0391, 2016
- Dlugokencky E. J., Harris J. M., Chung Y. S., Tans P. P., Fung I., The relationship between the methane seasonal cycle and regional sources and sinks at Tae-ahn Peninsula, Korea. Atmos. Environ. 27A:2115–2120. 1993
- Dlugokencky, E. J., L. P. Steele, P. M. Lang and K. A. Masarie, Atmospheric CH<sub>4</sub> at Mauna Loa and Barrow Observatories: presentation and analysis of in situ measurements, J. Geophys. Res., 100(D11), 23103–23113, doi:10.1029/95jd02460, 1995
- Fang, S.-X., L.-X. Zhou, K. A. Masarie, L. Xu, and C. W. Rella, Study of atmospheric CH<sub>4</sub> mole fractions at three WMO/GAW stations in China, JOURNAL OF GEOPHYSICAL RESEARCH: ATMOSPHERES, 118, 4874–4886, 2013
- Fang, S. X., P. P. Tans, M. Steinbacher, L. X. Zhou, and T. Luan, Comparison of the regional CO<sub>2</sub> mole fraction filtering approaches at a WMO/GAW regional station in China. Atmos. Meas. Tech., 8, 5301–5313, doi:10.5194/amt-8-5301-2015, 2015



- Graven, H.D., Guilderson, T.P., and Keeling, R.F.: Observations of radiocarbon in CO<sub>2</sub> at La Jolla, California, USA 1992–2007: Analysis of the long-term trend, *J.Geophys.Res.*,117,D02302, <https://doi.org/10.1029/2011JD016533>, 2012
- Higuchi, K., Worthy, D., Chan, D., and Shashkov, A.: Regional source/sink impact on the diurnal, seasonal and inter-annual variations in atmospheric CO<sub>2</sub> at a boreal forest site in Canada, *Tellus B*, 55, 115–125, 2003.
- 5 IPCC, 2021: Summary for Policymakers. In: *Climate Change 2021: The Physical Science Basis. Contribution of Working Group I to the Sixth Assessment Report of the Intergovernmental Panel on Climate Change* [Masson-Delmotte, V., P. Zhai, A. Pirani, S. L. Connors, C. Péan, S. Berger, N. Caud, Y. Chen, L. Goldfarb, M. I. Gomis, M. Huang, K. Leitzell, E. Lonnoy, J.B.R. Matthews, T. K. Maycock, T. Waterfield, O. Yelekçi, R. Yu and B.
- 10 Zhou (eds.)]. Cambridge University Press. In Press
- Ito, A., S. Inoue and M. Inatomi, Model-based evaluation of methane emissions from paddy fields in East Asia, *Journal of Agricultural Meteorology* 78(2), 56-65, 2022
- Jackson, R. B., M. Saunio, P. Bousquet, J. G. Canadell, B. Poulter, A. R. Stavert, P. Bergamaschi, Y. Niwa, A. Segers and A. Tsuruta, Increasing anthropogenic methane emissions arise equally from agricultural and fossil fuel
- 15 sources, *Environ. Res. Lett.* 15, <https://doi.org/10.1088/1748-9326/ab9ed2>, 2020
- Janssens-Maenhout, G.; M. Crippa, D. Guizzardi, M. Muntean, E. Schaaf, F. Dentener, P. Bergamaschi, V. Pagliari, J. G. J. Olivier, J. A. H. W. Peters, J. A. van Aardenne, S. Monni, U. Doering, A. M. R. Petrescu, E. Solazzo, G. D. Oreggioni: EDGAR v4.3.2 Global Atlas of the three major greenhouse gas emissions for the period 1970–2012, *Earth Syst. Sci. Data*, 11, 959–1002, <https://doi.org/10.5194/essd-11-959-2019>, 2019
- 20 Kai, F. M., S. C. Tyler, J. T. Randerson, and D. R. Blake (2011), Reduced methane growth rate explained by decreased Northern Hemisphere microbial sources, *Nature*, 476(7359), 194– 197., 2011
- Kim, H.-S., Yong S. Chung, P. P. Tans, Dlugokencky, E. J., Decadal trends of atmospheric methane in East Asia from 1991 to 2013, *Air Qual Atmos Health*, 8, 293-298, 2015
- Kenea, S. T., H. Lee, S. Joo, S. Li, L. D. Labzovskii, C.-Y. Chung, Y.-H. Kim, Interannual Variability of Atmospheric CH<sub>4</sub> and Its Driver Over South Korea Captured by Integrated Data in 2019, *Remote Sens.* 2021, 13, 2266. <https://doi.org/10.3390/rs13122266>, 2021
- 25
- Lan, X., E. G. Nisbet, E. J. Dlugokencky and S. E. Michel, What do we know about the global methane budget? Results from four decades of atmospheric CH<sub>4</sub> observations and the way forward, *Philos. Trans. R. Soc. A.*, <https://doi.org/10.1098/rsta.2020.0440>, 2021
- 30
- Lee, H., Han, S.-O., Ryoo, S.-B., Lee, J.-S., and Lee, G.- W.: The measurement of atmospheric CO<sub>2</sub> at KMA GAW regional stations, its characteristics, and comparisons with other East Asian sites, *Atmos. Chem. Phys.*, 19, 2149–2163, <https://doi.org/10.5194/acp-19-2149-2019>, 2019.
- Lee, S., H. Lee, S. Kim, Y.-H., Kim, Inter-comparison Experiment for Korea GAW Network to Improve the GHGs Measurement Quality, *Journal of Korean Society for Atmospheric Environment*, 37, 5, 790-802, 2021
- 35
- Li, S., S. Park, J.-Y. Lee, K.-J. Ha, M.-K. Park, C. O. Jo, H. Oh, J. Mühle, K.-R. Kim, S. A. Montzka, S. O'Doherty, P. B. Krummel, E. Atlas, B. R. Miller, F. Moore, R. F. Weiss, S. C. Wofsy, Chemical evidence of interhemispheric air mass intrusion into the Northern Hemisphere mid-latitudes, *Scientific Report*, DOI:10.1038/s41598-018-22266-0, 2018



- Liu, G., S. Peng, X. Lin, P. Ciais, X. Li, Y. Xi, Z. Lu, J. Chang, M. Saunio, Y. Wu, P. Patra, N. Chandra, H. Zeng, and S. Piao, Recent Slowdown of Anthropogenic Methane Emissions in China Driven by Stabilized Coal Production, *Environ. Sci. Technol. Lett.* 8, 739–746, <https://doi.org/10.1021/acs.estlett.1c00463>, 2021
- 5 Lowe, D. C., P. R. Guenther, and C. D. Keeling, The concentration of atmospheric carbon dioxide at Baring Head, New Zealand. *Tellus*, 31, 58-67, doi:10.1111/j.2153-3490.1979.tb00882.x. 1979
- Prinn, R. G., J. Huang, R. F. Weiss, D. M. Cunnold, P. J. Fraser, P. G. Simmonds, A. McCulloch, C. Harth, S. Reimann, P. Salameh, S. O'Doherty, R. H. J. Wang, L. W. Porter, B. R. Miller, P. B. Krummel, Evidence for variability of atmospheric hydroxyl radicals over the past quarter century, *Geophys. Res. Lett.*, 32, L078029, 2005
- 10 Poirot, R. L., and Wishinski, P. R. Long-term ozone trajectory climatology for the eastern US. Part 2: Results. *United States: N. p.*, 1998. Web.
- Rella, C. W., Chen, H., Andrews, A. E., Filges, A., Gerbig, C., Hatakka, J., Karion, A., Miles, N. L., Richardson, S. J., Steinbacher, M., Sweeney, C., Wastine, B., and Zellweger, C.: High accuracy measurements of dry mole fractions of carbon dioxide and methane in humid air, *Atmos. Meas. Tech.*, 6, 837?860, doi:10.5194/amt-6-837-2013, 2013.
- 15 Seo W., H. Lee, Y.-H. Kim, Revision of 22-year Records of Atmospheric Baseline CO<sub>2</sub> in South Korea: Application of the WMO X2019 CO<sub>2</sub> Scale and a New Baseline Selection Method (NIMS Filter), *Atmosphere. Korean Meteorological Society*, 31, 5, 1-14, 2021
- Sherwood, O. A., Schwietzke, S., Arling, V. A., & Etiope, G. Global inventory of gas geochemistry data from fossil fuel, microbial and burning sources, version 2017. *Earth System Science Data*, 9(2), 639–656. <https://doi.org/10.5194/essd-9-639-2017>, 2017
- 20 Shuang-Xi Fang, Ling-Xi Zhou, Kenneth A. Masarie, Lin Xu, and Chris W. Rella, Study of atmospheric CH<sub>4</sub> mole fractions at three WMO/GAW stations in China, *Journal of Geophysical Research: Atmospheres*, VOL. 118, 4874–4886, doi:10.1002/jgrd.50284, 2013
- Thoning K, W., P. P. Tans, and W. D. Komhyr: Atmospheric Carbon dioxide at Mauna Loa Observatory 2. Analysis of the NOAA GMCC Data, 1984-1985. *J. Geophys. Res.* 8549-8565, 1989
- 25 Turnbull, J.C., Rayner, P., Miller, J., Newberger, T., Ciais, P. and Cozic, A.: On the use of <sup>14</sup>CO<sub>2</sub> as a tracer for fossil fuel CO<sub>2</sub>: 30 Quantifying uncertainties using an atmospheric transport model, *J. Geophys. Res.*, 114, D22302, <https://doi.org/10.1029/2009JD012308>, 2009
- 30 Varga, T., R. E. Fisher, J. L. France, L. Haszpra, A. J. T. Jull, D. Lowry, I. Major, M. Molnar, E. G. Nisbet, and E. Laszlo, Identification of Potential Methane Source Regions in Europe Using  $\delta^{13}\text{CCH}_4$  Measurements and Trajectory Modeling, *Journal of Geophysical Research: Atmospheres*, 126, e2020JD033963. <https://doi.org/10.1029/2020JD033963>, 2021
- Verhulst, K. R., A. Karion, J. Kim, P. K. Salameh, R. F. Keeling, S. Newman, J. Miller, C. Sloop, T. Pongetti, P. Rao, C. Wong, F. M. Hopkins, V. Yadav, R. F. Weiss, R. M. Duren, and C. E. Miller, Carbon dioxide and methane measurements from the Los Angeles Megacity Carbon Project – Part 1: calibration, urban enhancements, and uncertainty estimates, *Atmos. Chem. Phys.*, 17, <https://doi.org/10.5194/acp-17-8313-2017>, 8313-8341, 2017
- 35 Wang, F., S. Maksyutov, R. Janardan, A. Tsuruta, A. Ito, I. Morino, Y. Yoshida, Y. Tohjima, J. W. Kaiser, G. Janssens-Maenhout, X. Lan, I. Mammarella, J. V. Lavric and T. Matsunaga, Interannual variability on methane emissions





- in monsoon Asia derived from GOSAT and surface observations, *Environ. Res. Lett.*, 16, <https://doi.org/10.1088/1748-9326/abd352>, 2021
- Winderlich, J., H. Chen, C. Gerbig, T. Seifert, O. Kolle, J. V. Lavric, C. Kaiser, A. Höfer, and M. Heimann, Continuous low-maintenance CO<sub>2</sub>/CH<sub>4</sub>/H<sub>2</sub>O measurements at the Zotino Tall Tower Observatory (ZOTTO) in Central Siberia, *Atmos. Meas. Tech.*, 3, 1113–1128, 2010
- 5
- WMO: Greenhouse Gas Bulletin, The State of Greenhouse Gases in the Atmosphere Based on Global Observations through 2020, No.17, 25 October 2021
- Worthy, D. E. J., I. Levin, N. B. A. Trivett, A. J. K. Kuhlmann, J. F. Hopper, and M. K. Ernst, Seven years of continuous methane observations at a remote boreal site in Ontario, Canada, *J. Geophys. Res.*, 103(D13), 15995–16007, doi:10.1029/98JD00925., 1998
- 10
- Zhao, Cong Long and Tans, Pieter P. : Estimating uncertainty of the WMO mole fraction scale for carbon dioxide in air. *Journal of Geophysical Research*, 111, D08S09, doi:10.1029/2005JD006003, 2006
- Zhou, L. X., D. E. J. Worthy, P. M. Lang, M. K. Ernst, X. C. Zhang, Y. P. Wen, and J. L. Li (2004), Ten years of atmospheric methane observations at a high elevation site in Western China, *Atmos. Environ.*, 38(40), 7041–7054, doi:10.1016/J.atmosenv.2004.02.072.
- 15
- Zhang F., L.-X. Zhou, L. Xu, Temporal variation of atmospheric CH<sub>4</sub> and the potential source regions at Waliguan, China, *Earth Sciences*, 56, 727–736, doi: 10.1007/s11430-012-4577-y, 2013
- Zhang, X., Hong Jiang , Yueqi Wang , Ying Han , M. Buchwitz ,O. Schneising & J. P. Burrows, Spatial variations of atmospheric methane concentrations in China, *International Journal of Remote Sensing*, 32:3, 833-847, DOI:10.1080/01431161.2010.517804, 2011
- 20